CHINESE OPTICS LETTERS

Vol. 20, No. 8 | August 2022

Temperature insensitive multi-channel light amplification systems on SOI platform

Junhu Zhou (周军虎)[1], Jie You (尤 洁)[2**], Hao Ouyang (欧阳昊)[1], Runlin Miao (苗润林)[1], Xiang'ai Cheng (程湘爱)[1], and Tian Jiang (江 天)[1,3*]

[1] College of Advanced Interdisciplinary Studies, National University of Defense Technology, Changsha 410073, China

[2] Defense Innovation Institute, Academy of Military Sciences PLA China, Beijing 100071, China

[3] Beijing Institute for Advanced Study, National University of Defense Technology, Beijing 100020, China

*Corresponding author: tjiang@nudt.edu.cn

**Corresponding author: jieyou1991@hotmail.com

Received January 23, 2022 | Accepted April 28, 2022 | Posted Online May 26, 2022

We present a theoretical analysis of a novel multi-channel light amplification photonic system on chip, where the nonlinear Raman amplification phenomenon in the silicon (Si) wire waveguide is considered. Particularly, a compact and temperature insensitive Mach–Zehnder interferometer filter working as demultiplexer is also exploited, allowing for the whole Si photonic system to be free from thermal interference. The propagation of the multi-channel pump and Stokes lights is described by a rigorous theoretical model that incorporates all relevant linear and nonlinear optical effects, including the intrinsic waveguide optical losses, first- and second-order frequency dispersion, self-phase and cross-phase modulation, phase shift and two-photon absorption, free-carriers dynamics, as well as the inter-pulse Raman interaction. Notably, to prevent excessive drift of the transmission window of the demultiplexer caused by ambient temperature variations and high thermo-optical coefficient of Si, an asymmetric waveguide width is adopted in the upper and lower arms of each Mach–Zehnder interferometer lattice cell. A Chebyshev half-band filter is utilized to achieve a flat pass-band transmission, achieving a temperature sensitivity of < 1.4 pm/K and over 100 K temperature span. This all-Si amplifier shows a thermally robust behavior, which is desired by future Si-on-insulator (SOI) applications.

Key words: silicon-on-insulator; multi-channel; amplification; temperature.

DOI: 10.3788/COL202220.081301

1. Introduction

The silicon-on-insulator (SOI) platform is the most promising route toward seamlessly realizing optical devices in chip-level communication circuits[1,2]. Especially, the silicon (Si) waveguide has exhibited distinguished optical properties encompassing a broadband transparency window, high index contrast, and excellent compatibility with CMOS electric circuitries[3–5]. However, Si-based amplifiers remain puzzles because of the indirect band gap. Transfer printing is developed for simultaneous transfer of multiple processed III–V materials from the source III–V wafer to the target SOI wafer[6,7]. Though this technology allows for efficient use of III-V material as the optical gain medium, it deviates greatly from the CMOS industry, resulting in the expensive cost of the proposed circuit. On the other hand, Er^{3+}-doped materials have inspired significant studies exploring various Si-based light amplifiers, especially ones employing Er^{3+}-doped waveguides in integrated circuits[8,9]. Unfortunately, it is not feasible to realize high Er^{3+} concentrations for high gain over a short length, due to the limitations of Er^{3+} solid solubility.

Benefiting from the large nonlinearity of Si, stimulated Raman scattering (SRS) is used to achieve tunable light amplification. In particular, SOI wire waveguides have performed experimentally to prove the validity of signal amplification, modulation, and frequency conversion[10,11]. For the waveguides that have a cross section of less than 0.1 μm^2, the light confinement is strongly enhanced; therefore, additional losses contributed by two-photon absorption (TPA) effects, free carrier (FC), group-velocity (GV) dispersion, self-phase modulation (SPM), and cross-phase modulation (XPM) are improved by strong optical injection, impairing the signal quality but also reducing the characteristic lengths of dispersion[12]. In wavelength division multiplexing applications, photogenerated FCs induce extra signal crosstalk, which is another aspect of a detrimental effect[13]. Thus, we need a rigorous model to calculate the result of pulsed SRS.

Another imperative limitation of SOI devices is the high thermo-optic (TO) coefficient of Si ($1.86 \times 10^{-4}\ \mathrm{K}^{-1}$). There can be significant change in the refractive index with temperature difference. Temperature sensitivity of a conventional Mach–Zehnder interferometer (MZI) is 80 pm/K[14,15]. A Si photonic circuit therefore needs temperature stabilization or compensation for the TO effect of Si. One method is the introduction of materials with negative TO coefficients as cladding, such as titanium dioxide or polymers[16], but there is an inevitable increase process complexity, and it is not always worthy to incorporate such materials in a CMOS-like process flow.

Here, we conduct a profound analysis of multi-channel Raman-mediated pulse amplification in a Si photonic system, which also owns remarkable temperature insensitive demultiplexing characteristics. Importantly, the amplification of desired Stokes light provides a potential avenue to deal with the excessive attenuation of optical signals. Meanwhile, we also pay loads of attention to compensate the wavelength drift, which is raised by heat accumulation or circumstance variation. By designing the asymmetric waveguide arm in the MZI, it is possible to effectively reduce the sensitivity of the entire optical amplification system to ambient temperature up to 400 K. In addition, the principle of an optical half-band filter is used to restrain the crosstalk of adjacent channels and further improve the thermal tolerance[17]. Notably, our proposed temperature insensitive multi-channel light amplification photonic system can be realized just using the standard SOI fabricating process, rather than the expensive customized manufacturing process.

2. Result and Discussion

Our multi-channel light amplification system is depicted in Fig. 1. The Si wire waveguide is buried in SiO_2 cladding with a uniform cross section. The proposed system consists of N pump lasers and a noise seed source, a vertical coupling grating, a Si wire waveguide, a thermal tolerance demultiplexer, and N optical detectors. By vertical coupling, the pump lights and noise seed, which represent either a weak signal or a signal buried in noise, will enter the Si wire waveguide and interact with each other via optical phonons[18]. A thermal tolerance filter is connected to the end of the wire waveguide. Finally, the output signals of the wire waveguides are demultiplexed and analyzed using a power meter.

First, we calculate the dispersion coefficients and mode profile of the Si waveguide by using the finite element method (FEM). Figure 2 presents the modal dispersion in the C band. The materials refractive index $n(\lambda)$ at diverse temperature is given by the Sellmeier model[19]:

$$n^2(\lambda,T) - 1 = \sum_{i=1}^{m} \frac{S_i(T)\lambda^2}{\lambda^2 - \lambda_i^2(T)},$$

where S_i is the strengths of the resonance features in the material at wavelengths λ_i. For Si and SiO_2, the material constants are measured by Refs. [20,21], respectively. In this article, we only consider the TE_0 mode. Propagation constant β is extracted from the mode refractive index and presented in Fig. 2(a). Modal dispersion is used to calculate the higher-order dispersion coefficients $\beta_i(\omega) = \mathrm{d}^i\beta(\omega)/\mathrm{d}\omega^i$, where ω represents angular frequency, and i is differential order. Figures 2(b) and 2(c) show the first- and second-order dispersion coefficients that are derived from Fig. 2(a). The frequency dispersion of group index n_g is captured by Fig. 2(d). The multi-channel optical pulse propagation and Raman-mediated pulse interaction can be characterized by an array of coupled nonlinear Schrodinger equations and a rate equation[22]:

$$\begin{aligned} j\frac{\partial u_i}{\partial z} + j\left(\frac{1}{v_{g,i}} - \frac{1}{v_{g,\mathrm{ref}}}\right)\frac{\partial u_i}{\partial t} - \frac{\beta_{2,i}}{2}\frac{\partial^2 u_i}{\partial t^2} &= -\frac{\omega_i \delta n_{\mathrm{FC}} \kappa_i}{n v_{g,i}} u_i \\ -\frac{jc\kappa_i}{2n v_{g,i}}(\alpha_{\mathrm{in}} + \alpha_{\mathrm{FC}})u_i - \left(\gamma_i |u_i|^2 + 2\sum_{m\neq i}\gamma_{im}|u_m|^2\right) \\ \times u_i - 2\gamma_{im}^r |u_m|^2 u_i, \end{aligned} \tag{1}$$

$$\frac{\partial N}{\partial t} = -\frac{N}{\tau_c} + \sum_{i,m} D_{im}|u_i|^2|u_m|^2, \tag{2}$$

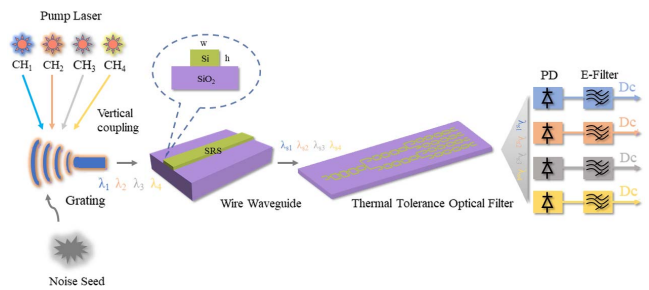

Fig. 1. Multi-channel Si photonic system. CH_i represents the corresponding pump light λ_i and Stokes light λ_{si}. Si wire waveguide height h = 220 nm, width w = 450 nm.

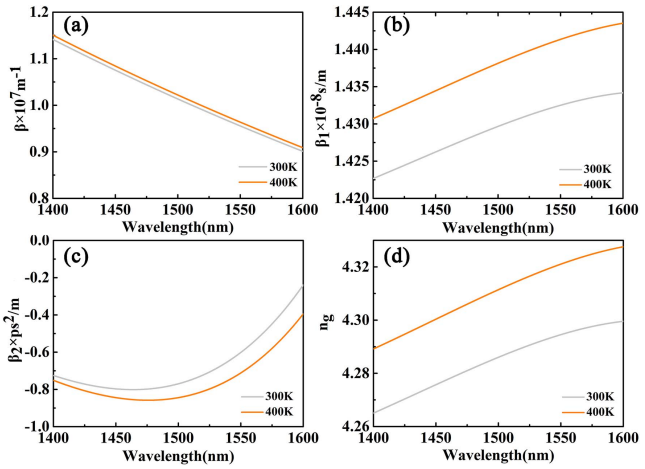

Fig. 2. Dispersion coefficients of wire waveguides. (a) Propagation constant. (b) First-order dispersion coefficient. (c) Second-order dispersion coefficient. (d) Group refractive index.

where $u_i(z,t)$ is the ith pulse envelope for the four-channel light amplification system, i and m are taken from 1 to 8 including four pump lights and four Stokes lights, and the interaction between them is demonstrated by the cross term γ_{im} and u_m. z and t are the propagation length and the time at the reference central wavelength moving with GV $v_{g,\mathrm{ref}}$, respectively. $t = t_0 - z/v_{g,\mathrm{ref}}$, where t_0 is the physical time. ω_i is the carrier frequency of the ith wavelength, κ_i represents the overlap between the active area of the waveguide and the TE_0 mode. α_{in} is the intrinsic absorption coefficient, which is set to $1\,\mathrm{dB\,cm^{-1}}$. $\tau_c = 0.5$ ns is the FC relaxation time[13]. δn_{FC} and α_{FC} are the refractive index change and FC loss coefficient induced by FCs. Based on a Drude model, those two quantities are computed by

$$\delta n_{\mathrm{FC}} = -\frac{e^2}{2\epsilon_0 n\omega^2}\left[\frac{\Delta N_e}{m^*_{\mathrm{ce}}} + \frac{(\Delta N_h)^{0.8}}{m^*_{\mathrm{ch}}}\right], \tag{3}$$

$$\alpha_{\mathrm{FC}} = \frac{e^3}{\epsilon_0 cn\omega^2}\left(\frac{\Delta N_e}{\mu_e m^{*2}_{\mathrm{ce}}} + \frac{\Delta N_h}{\mu_h m^{*2}_{\mathrm{ch}}}\right). \tag{4}$$

e is the charge of the electron; $m^*_{\mathrm{ce}} = 0.26m_0$ and $m^*_{\mathrm{ch}} = 0.39m_0$ are the effective masses of the electrons and holes. ΔN_e and ΔN_h are the nonequilibrium carrier density. μ_e and μ_h are the carriers' mobility. Due to the strongly enhanced mode confinement within the small transverse dimensions, the effective third-order nonlinearity is sensitive to the distribution of power densities in the cross section, which is computed by the overlap integral of the mode field profile. The nonlinear coefficients γ_i, γ_{im}, and γ^r_{im} in Eq. (1) are given by

$$\gamma_i = \frac{3\omega_i\epsilon_0}{16v^2_{g,i}}\frac{\Gamma_i}{W_i^2}, \tag{5}$$

$$\gamma_{im} = \frac{3\omega_i\epsilon_0}{16v_{g,i}v_{g,m}}\frac{\Gamma_{im}}{W_i W_m}, \tag{6}$$

$$\gamma^r_{im} = \frac{3\omega_i\epsilon_0}{16v_{g,i}v_{g,m}}\frac{\Gamma^r_{im}}{W_i W_m}. \tag{7}$$

Here, W_i is the optical mode energy per unit length, which is calculated by

$$W_i = \frac{1}{4}\int_S [\epsilon(r)|e(r,\omega_i)|^2 + u_0|h(r,\omega_i)|^2]\mathrm{d}S, \tag{8}$$

where $e(r,\omega_i)$ and $h(r,\omega_i)$ are the electric and magnetic fields computed by FEM, respectively. Furthermore, Γ_i, Γ_{im}, and Γ^r_{im} are mode-mediated effective nonlinear susceptibilities coefficients, which can be defined by certain weighted integrals of the corresponding tensor susceptibilities $\hat{\chi}$ over the transverse area of the waveguide:

$$\Gamma_i = \int_S e_i^*(r)\hat{\chi}^{(3)}(\omega_i, -\omega_i, \omega_i)\vdots e_i(r)e_i^*e_i(r)\mathrm{d}S, \tag{9}$$

$$\Gamma_{im} = \int_S e_i^*(r)\hat{\chi}^{(3)}(\omega_m, -\omega_m, \omega_i)\vdots e_m(r)e_m^*e_i(r)\mathrm{d}S, \tag{10}$$

$$\Gamma^r_{im} = \int_S e_i^*(r)\hat{\chi}^r(-\omega_r)\vdots e_m(r)e_m^*e_i(r)\mathrm{d}S. \tag{11}$$

In Eq. (11), ω_r is the Raman frequency, which is contingent upon the frequency of the optical phonons. The scattered Stokes signal is enlarged by a down shift of pump frequency, where the frequency shift is $\omega_r \cong 15.6$ THz for crystalline Si[19]. Finally, the parameter D_{im} in rate Eq. (2) calibrates the rate of optical energy transfer to the FC:

$$D_{im} = \begin{cases} \frac{\gamma_i''}{\hbar\omega_i A} & i = m \\ \frac{4\gamma_{im}''}{\hbar(\omega_i+\omega_m)A} & i \neq m \end{cases}. \tag{12}$$

Here, A is the effective transverse area of the TE_0 mode where FCs are generated. In order to simplify the calculation, we assumed $A = w \times h$. The symbol γ' (γ'') stands for the real (imaginary) part of the complex number γ.

Four Stokes lights are choired to the wavelength of $\lambda_{s1} = 1549.2$, $\lambda_{s2} = 1550.0$, $\lambda_{s3} = 1550.8$, and $\lambda_{s4} = 1551.6$ nm. Therefore, the central wavelength of pump lights induced by Raman frequency should be $\lambda_1 = 1433.63$, $\lambda_2 = 1434.31$, $\lambda_3 = 1435.00$, and $\lambda_4 = 1435.68$ nm. λ_4 is presumed as the reference wavelength. The peak powers of pump pulses and initial signals are set to 500 mW and 0.1 mW. As shown in Fig. 3(a), four pump pulses with a temporal width of 30 ps are simultaneously coupled into the wire waveguide. The SRS process almost instantaneously occurs at the head of the wire waveguide, as depicted in Fig. 3(b). The length of the wire waveguide is selected to be 3 mm. Figures 3(c) and 3(d) show the normalized pulse profile of CH1 (the first channel of amplifier) at the waveguide position of 0 and 3 mm. Owing to the Raman interaction, the pump pulse has a significant attenuation and distortion in the temporal shape. At the same time, the peak amplitude of the Stokes pulse is amplified 37 times.

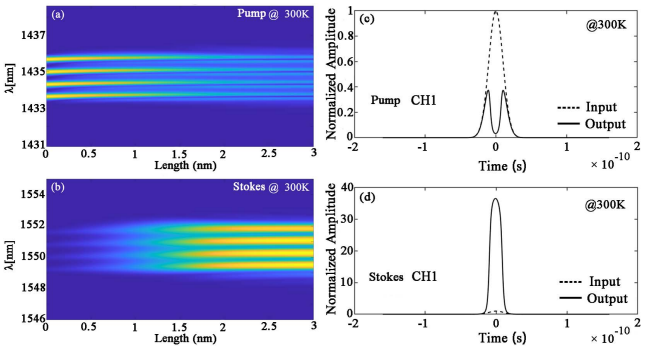

Fig. 3. Four-channel SRS effect. (a) The propagation of pump lights. (b) The propagation of Stokes lights. (c) Input (dash line) and output (solid line) profiles of CH1 pump pulse. (d) Input (dash line) and output (solid line) profiles of CH1 Stokes pulse.

There is a notable drift in the frequency domain where the outputs are diverse from the original designed wavelength. The actual emitted wavelengths of the wire waveguide are 1549.55, 1550.30, 1551.10, and 1551.85 nm, respectively. Therefore, the operated wavelengths of the demultiplexer are modified correspondingly. The shift toward a higher Raman induced frequency occurs when the input pulse is relatively short, and its high frequency components can pump the low frequency components by SRS, thus the energy of the pulse is transferring to the red side. When the pulse spectrum shifts happen through intra-pulse Raman scattering, the pulse propagation is slowed down because of the decreased GV at longer wavelengths in the $\beta_2 < 0$ case[23]. This deacceleration is responsible for the bent trajectory of the pulse seen in Figs. 3(a) and 3(b).

Figure 4 shows the 3D light propagation result, where the coherent generation of the Raman signal is clearly demonstrated. As the intrinsic loss is set to 1 dB/cm, the power in the Raman pulse increases to a threshold value at a 0.7 mm distance, and then the interaction with the pump pulse turns strong enough to change its profile, as depicted in Fig. 4(a). Meanwhile, the Raman pulse rises rapidly from a weak signal, as shown in Fig. 4(b). Finally, the outputs of the amplified four channels Stokes lights are displayed in Fig. 4(c). These two curves overlap almost completely, indicating that the thermal stability of Raman amplification process needs no more optimization.

In fact, the high TO coefficient of Si does critically disturb the system performance because of the thermal sensitivity of demultiplexers. The common architecture of the two stages MZIs demultiplexer is shown in Fig. 5(a). The corresponding free spectral ranges (FSRs) of the first and second stage MZIs are set to be 1.54 nm and 3.08 nm, respectively. The FSR of the individual MZI is inversely proportional to the delay length:

$$\mathrm{FSR} = \frac{\lambda^2}{n_g \Delta L}, \tag{13}$$

where λ is the center wavelength of interest, and ΔL is the physical path length difference between the longer and shorter arms of the MZIs[24]. We still use the 450 nm waveguides and select the modified λ_{s2} as the center wavelength. Using Eq. (13), the ΔL is computed to be 352.48 and 176.13 μm for the first and second stage MZIs, respectively.

The power coupling coefficient (θ^2) of the directional coupler (DC) should be intelligently exploited. Figure 5(b) is a common DC with 200 nm gap and 450 nm waveguide width. In the circuit presented in Fig. 5(a), all DCs have a θ^2 of 0.5, which is responsible for a uniform distribution of the electric field seen in Fig. 5(b). At 300 K, the corresponding coupling length is 9.4 μm. So far, a temperature sensitive demultiplexer is determined by the ΔL and coupling length of the DCs. The transmission of the demultiplexer at 300 K is shown in Fig. 5(c). When the temperature rises to 400 K, we revised the effective refractive index of the waveguides and recalculated the S parameters of DCs by changing the refractive index of Si and SiO_2. It is worth noting that the coupler length of DCs and ΔL are maintained. The transmission of the demultiplexer at 400 K is shown in Fig. 5(d). All channels are red shifted, and the wavelengths of the output ports are confused. Based on the results of Figs. 4(c), 5(c), and 5(d), the terminal output is shown in Fig. 6. At a temperature of 400 K, the peak wavelengths of CH1, CH2, and CH3 deviate from the designed center wavelength by ~0.83 nm, owing to the red shift of the operation wavelength. The blue shift in Fig. 6(d) actually comes from the periodicity of the transmission window. This wide range of output wavelength drift caused by temperature changes will greatly limit the performance of this optical amplification system.

To reduce the impact of temperature, we introduce both the optical half-band filter architecture and asymmetric waveguide width in cascaded MZIs. Figure 7(a) shows a cascaded Mach–Zehnder-like lattice unit, which is abstractly simplified as a block in Fig. 7(b). Chebyshev half-band filters possess a wider 1 dB bandwidth, which can help effectively suppress the change in transmission signals when the wavelength shift has occurred. A synthesis algorithm based on MZIs for arbitrary FIR filters is developed in Ref. [14]. The key parameters θ_i, φ_i, and ΔL are marked in the picture, where φ_i is the extra phase shift.

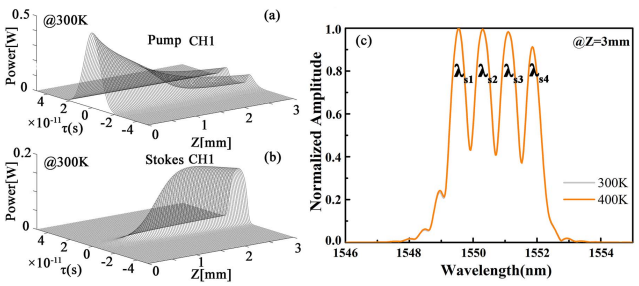

Fig. 4. Transmission in the wire waveguide. (a) The propagation of 1435.68 nm pump pulse. (b) The propagation of 1551.60 nm Stokes pulse. (c) The transmission of the enlarged four-channel Stokes lights at 300 K and 400 K, respectively.

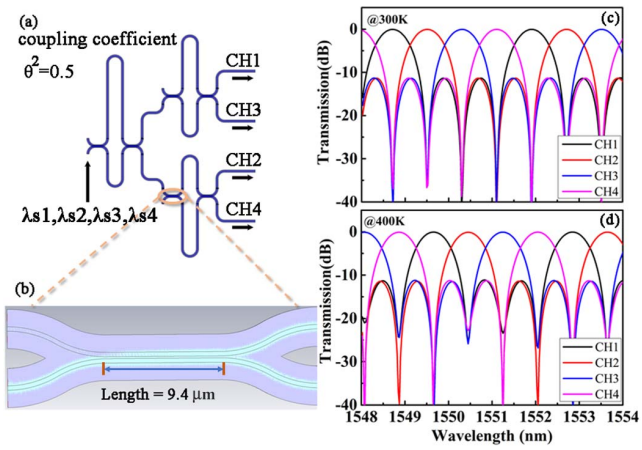

Fig. 5. Temperature sensitive de-multiplexer. (a) The two-stage cascaded Mach–Zehnder wavelength filter. (b) Electric field intensity profile for the DC at a wavelength of 1.55 μm. (c) Transmission of de-multiplexer displayed in (a) at 300 K. (d) Transmission of de-multiplexer displayed in (a) at 400 K.

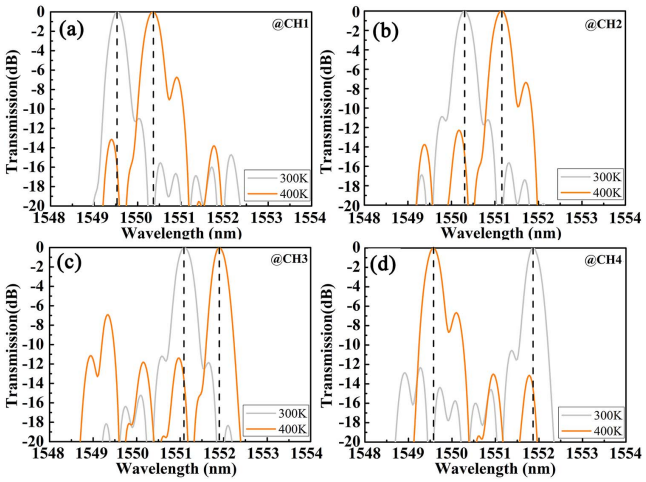

Fig. 6. Transmission of the enlarged Stokes light through the four-channel de-multiplexer. (a) CH1 output port. (b) CH2 output port. (c) CH3 output port. (d) CH4 output port.

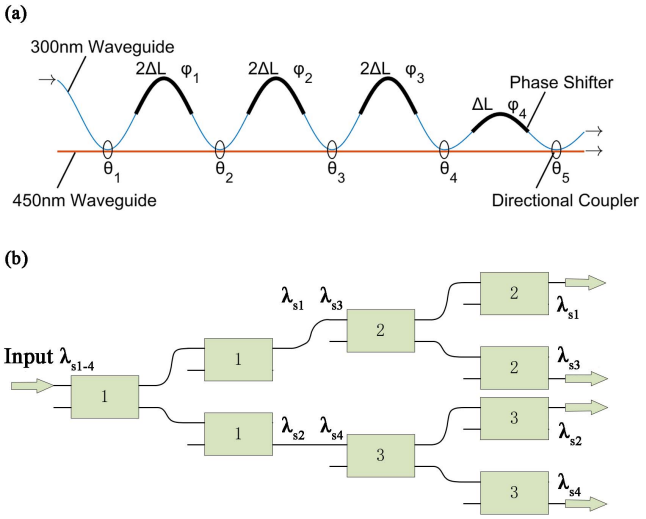

Fig. 7. Proposed temperature insensitive flat pass-band filter. (a) Single cell of the cascaded Mach–Zehnder-like lattice filters. (b) The anti-thermal four-channel wavelength splitting filters.

For the Chebyshev optical half-band filters, θ_i and φ_i are listed in Table 1.

At 300 K, the DC coupling length corresponding to the power coupling coefficient in Table 1 is 13.9, 9.1, 17.4, 1.35, and 9.4 μm in turn. To be rigorous, we also consider the performance of DCs at 400 K. Figure 7(a) shows a design of combining wide and narrow waveguides in different arms. The two arms of the MZIs have a different TO coefficient. By selecting appropriate arm lengths, the temperature dependence of both the arms can be made to cancel each other out. Three of the same blocks are cascaded for restraining the crosstalk, as shown in Fig. 7(b). The thermal sensitivity of a standard MZI can be expressed as

$$\frac{\mathrm{d}\lambda}{\mathrm{d}T}=\frac{\lambda}{n_g}\frac{\mathrm{d}n_{\mathrm{eff}}}{\mathrm{d}T}, \tag{14}$$

where n_{eff} is the waveguide effective refractive index. For the projected structure with different waveguides in the two arms, the modified expressions of Eqs. (13) and (14) are

$$\mathrm{FSR}=\frac{\lambda^2}{n_{g,1}L_1-n_{g,2}L_2}, \tag{15}$$

$$\frac{\mathrm{d}\lambda}{\mathrm{d}T}=\lambda\frac{\mathrm{TO}_1L_1-\mathrm{TO}_2L_2}{n_{g,1}L_1-n_{g,2}L_2}. \tag{16}$$

The wavelength shift versus temperature defined by Eq. (16) should be brought to zero. The TO coefficient and n_{eff} are shown in Fig. 8(a). In order to make a large difference in the TO coefficient between the two arms, thereby reducing the footprint, the waveguide widths are chosen to be 300 nm and 450 nm. The ratio of the TO coefficient of 450 nm and 300 nm waveguides is $\mathrm{TO}_{450}/\mathrm{TO}_{300}=1.28414$. Thus, $L_{300}/L_{450}=1.28414$. Putting this ratio into Eq. (15), the waveguide lengths are calculated to be $L_{300}=1933.853$ μm and $L_{450}=1505.946$ μm, respectively, in the first stage with FSR = 1.54 nm. The transmission window needs to be slightly adjusted to coincide with the center wavelength of each channel. Finally, the revised arm lengths of the first stage MZIs are $L_{300}=1933.82$ μm and $L_{450}=1505.946$ μm, which are halved for the second stage MZIs. The phase shift φ should be added in the form of extra length of the 300 nm waveguide. In the case of 400 K, the effective refractive index of waveguides is recalculated, and the impact of temperature on DCs is included. To estimate the insertion loss of the demultiplexer, we take into account the propagation losses of 2.6 dB/cm and 1.5 dB/cm for the 300 nm and 450 nm waveguides. The transmission function of the demultiplexer is displayed in Fig. 8(b), indicating an insertion loss of 7 dB. A flat pass-band response is obviously seen with a 1 dB bandwidth of 0.53 nm, which is 0.28 nm in Fig. 5. The red shift

Table 1. Chebyshev Optical Half-Band Filters.

θ_1^2	θ_2^2	θ_3^2	θ_4^2	θ_5^2	φ_1	φ_2	φ_3	φ_4
0.79	0.49	0.94	0.06	0.50	π	0	π	0

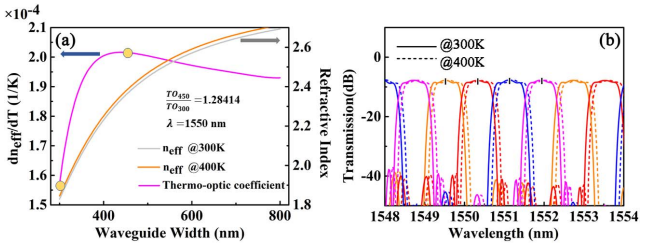

Fig. 8. (a) Simulated TO coefficients and effective refractive index. (b) Transmission of the designed temperature insensitive flat pass-band filter.

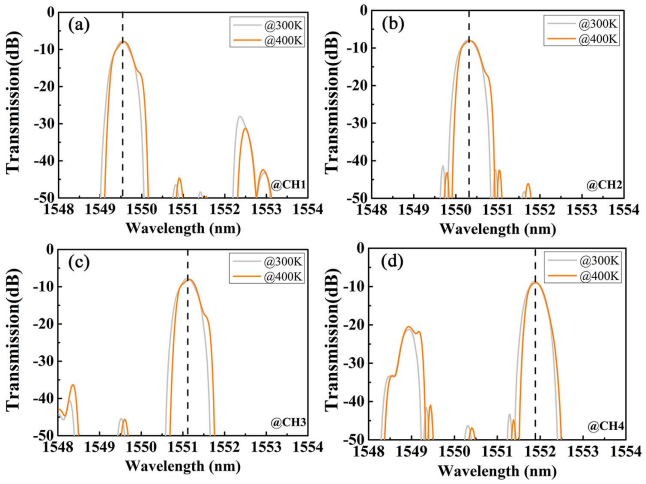

Fig. 9. Transmission of the enlarged Stokes lights through the anti-thermal four-channel de-multiplexer. (a) CH1 output port. (b) CH2 output port. (c) CH3 output port. (d) CH4 output port.

is greatly suppressed to 0.1 nm, and the value of the central wavelength of each channel remains unchanged. Compared with the common compact demultiplexer, it has better stop band rejection capability.

The results at different channels are presented in Fig. 9. One remarkable finding is that the transmission peaks are precisely located at the proposed wavelengths of 1549.55, 1550.30, 1551.10, and 1551.85 nm, respectively. A robust behavior is demonstrated by the almost coincident curves at 300 K and 400 K. At the central wavelength of each channel, this system perfectly avoids the impact of temperature by the flat band response and thermal insensitivity of the demultiplexer. In Figs. 9(b) and 9(c), the max crosstalk is −27 dB, which is consistent with the result shown in Fig. 8. The relatively large crosstalk that appears in Figs. 9(a) and 9(d) is due to the edge broadening of the spectrum in Fig. 4(c). Obviously, this large crosstalk can be eliminated simply by subsequent filtering. So far, we have designed a complete compact all-Si temperature insensitive multi-channel light amplification photonic system and confirmed all necessary structure and parameters. It is worth emphasizing that although we use pulsed light in our calculations in the Raman amplification process, monochromatic light or white light can also be used as the input to the system, as long as these beams contain the light information that needs to be amplified.

3. Conclusion

We demonstrate a theoretical computation of four-channel Raman-mediated light amplification in Si. Based on the Raman effects, we designed a thermal insensitive light amplification system on an SOI platform. All relative parameters are defined and shown in this article. The deliberate constructed system, which includes the architecture of a Chebyshev optical half-band filter and different waveguide widths in two arms, shows strong reliability, even the ambient variation is large. The highlight advantage of this system is the cost-effective passive compensation of wavelength shift without a complex fabrication process and energy-intensive active tuning. By increasing the output ports of the demultiplexer, this on-chip optical amplification system can scale up, which can be widely used for large-scale on-chip circuits as signal amplifiers, modulators, or photonic signal processors.

Acknowledgement

This work was supported by the National Natural Science Foundation of China (No. 11902358) and the Scientific Researches Foundation of National University of Defense Technology (Nos. ZK18-03-36 and ZK18-01-03).

References

1. Z. Chen and M. Segev, "Highlighting photonics: looking into the next decade," eLight **1**, 12 (2021).
2. P. Zhou, F. Zhang, Q. Guo, and S. Pan, "Linearly chirped microwave waveform generation with large time-bandwidth product by optically injected semiconductor laser," Opt. Express **24**, 18460 (2016).
3. D. Marpaung, C. Roeloffzen, R. Heideman, A. Leinse, S. Sales, and J. Capmany, "Integrated microwave photonics," Laser Photonics Rev. **7**, 506 (2013).
4. H. Subbaraman, X. Xu, A. Hosseini, X. Zhang, Y. Zhang, D. Kwong, and R. T. Chen, "Recent advances in silicon-based passive and active optical interconnects," Opt. Express **23**, 2487 (2015).
5. D. Yang, Y. Huang, T. Liu, X. Ma, and X. Ren, "Bias-free operational monolithic symmetric-connected photodiode array," Chin. Opt. Lett. **18**, 012501 (2018).
6. A. Yariv and X. Sun, "Supermode Si/III-V hybrid lasers, optical amplifiers and modulators: a proposal and analysis," Opt. Express **15**, 9147 (2007).
7. J. Zhang, B. Haq, J. O'Callaghan, G. Angieska, and R. Gunther, "Transfer-printing-based integration of a III-V-on-silicon distributed feedback laser," Opt. Express **26**, 8821 (2018).
8. A. D. Groote, P. Cardile, A. Z. Subramanian, A. M. Fecioru, and G. Roelkens, "Transfer-printing-based integration of single-mode waveguide-coupled III–V-on-silicon broadband light emitters," Opt. Express **24**, 13754 (2016).
9. D. Jonathan, B. Bradley, and M. Pollnau, "Erbium-doped integrated waveguide amplifiers and lasers," Laser Photonics Rev. **3**, 368 (2011).
10. P. Zhou, S. Wang, X. Wang, Y. He, and W. Kan, "High-gain erbium silicate waveguide amplifier and a low-threshold, high-efficiency laser," Opt. Express **26**, 16689 (2018).
11. T. Jiang, J. You, Z. Tao, Y. Luo, and X. Cheng, "BER evaluation in a multi-channel graphene-silicon photonic crystal hybrid interconnect: a study of fast- and slow-light effect," Opt. Express **28**, 17286 (2020).
12. R. L. Espinola, J. I. Dadap, R. M. Osgood, S. J. McNab, and Y. A. Vlasov, "Raman amplification in ultrasmall silicon-on-insulator wire waveguides," Opt. Express **12**, 3713 (2004).
13. P. Qi, Y. Luo, B. Shi, W. Li, D. Liu, L. Zheng, Z. Liu, Y. Hou, and Z. Fang, "Phonon scattering and exciton localization: molding exciton flux in two-dimensional disorder energy landscape," eLight **1**, 12 (2021).
14. S. Dwivedi, H. D'Heer, and W. Bogaerts, "Maximizing fabrication and thermal tolerances of all-silicon FIR wavelength filters," IEEE Photonics Technol. Lett. **27**, 871 (2015).
15. K. Zheng, W. Zou, L. Yu, N. Qian, and J. Chen, "Stability optimization of channel-interleaved photonic analog-to-digital converter by extracting of dual-output photonic demultiplexing," Chin. Opt. Lett. **18**, 012502 (2020).
16. T. Jie, P. Dumon, W. Bogaerts, H. Zhang, and R. Baets, "Athermal silicon-on-insulator ring resonators by overlaying a polymer cladding on narrowed waveguides," Opt. Express **17**, 14627 (2009).
17. F. Horst, W. Green, S. Assefa, S. M. Shank, Y. A. Vlasov, and B. J. Offrein, "Cascaded Mach–Zehnder wavelength filters in silicon photonics for low

loss and flat pass-band WDM (de-)multiplexing," Opt. Express **21**, 11652 (2013).
18. T. Balster, F. Tautz, V. Polyakov, H. Ibach, S. Sloboshanin, R. Ottking, and J. A. Schaefer, "Strong dispersion of the surface optical phonon of silicon carbide in the near vicinity of the surface Brillouin zone center," Surf. Sci. **600**, 2886 (2006).
19. S. Moghaddam and S. K. O'Leary, "A Sellmeier extended empirical model for the spectral dependence of the refractive index applied to the case of thin-film silicon and some of its more common alloys," J. Mater. Sci. Mater. Electron. **31**, 212 (2020).
20. B. J. Frey, D. B. Leviton, and T. J. Madison, "Temperature dependent refractive index of silicon and germanium," Proc. SPIE **6273**, 1235 (2006).
21. G. Ghosh and M. Endo, "Temperature-dependent Sellmeier coefficients and chromatic dispersions for some optical fiber glasses," J. Light. Technol. **12**, 1338 (1994).
22. J. Santhanam and G. P. Agrawal, "Raman-induced spectral shifts in optical fibers: general theory based on the moment method," Opt. Commun. **222**, 413 (2003).
23. L. Ma, J. Li, Z. Liu, Y. Zhang, N. Zhang, and S. Zheng, "Intelligent algorithms: new avenues for designing nanophotonic devices," Chin. Opt. Lett. **19**, 011301 (2021).
24. B. Bai, L. Pei, J. Zheng, T. Ning, and J. Li, "Ultra-short plasmonic polarization beam splitter-rotator using a bent directional coupler," Chin. Opt. Lett. **18**, 041301 (2020).